Frontiers in Heat and Mass Transfer (FHMT), 20, 11 (2023)
DOI: 10.5098/hmt.20.11

Global Digital Central
ISSN: 2151-8629

Frontiers in Heat and Mass Transfer

Available at www.ThermalFluidsCentral.org

EFFECT OF PARTICLE DIAMETER SIZE ON INTERNAL FLOW CHARACTERISTICS OF A SMALL SEWAGE PUMP

Yu-Liang Zhang[a,*], Dong-Yang Wu[b], Hai-Bing Cai[c], Can-Fei Wang[c], Fei-Wu[c], Shao-Han Zheng[d]

[a] *College of Mechanical Engineering, Quzhou University, Quzhou 324000, China*
[b] *Hangzhou Oxygen Plant Group Co., Ltd., Hangzhou 310014, China*
[c] *Zhejiang Testing & Inspection Institute for Mechanical and Electrical Products Quality Co., Ltd., Hangzhou 310014, China*
[d] *College of Mechanical Engineering, Zhejiang University of Technology, Hangzhou, 310023, China*

ABSTRACT

In this paper, based on the Mixture model, the numerical computations of the internal flow field in a sewage pump are carried out. Through numerical simulation, the turbulence flow characteristics in the sewage pump are obtained. Results show that when the particle diameter is 0.10 mm, the solid-phase concentration on the volute surface is high, and the wear is more severe. When the particle diameters are 0.15 mm and 0.20 mm, the solid-phase concentration on the volute surface is significantly higher, especially when the over-current cross-section enlarges constantly.

Keywords: *solid diameter; Mixture; numerical simulation; turbulence flow*

1. INTRODUCTION

Sewage pump is a key equipment in urban river dredging, wherein the size of particle diameter plays an important role on the hydraulic performance and internal flow characteristics of a solid–liquid two-phase flow sewage pump. Many scholars have conducted in-depth research and achieved fruitful results. For example, Engin *et al.* (2001) considered a semi-open impeller centrifugal pump as research object, compared the pump performance when the pump conveyed water, sand, and other hard materials, and developed an equation that expresses the effect of particle size on pump performance. Gandhi *et al.* (2002) studied the performance of a closed impeller centrifugal pump for conveying water, mortar, and zinc tailings with solid–liquid mixed media. Yuan *et al.* (2004) found a reflux in the inlet and a velocity slip between the two phases. The turbulent kinetic energy and dissipation rate at the boundary between the pressure surface and the suction surface reached the extreme value. Li *et al.* (2012) found that under the operating condition of small flow, the efficiency value increases slightly, the stable working area becomes small, and the optimal efficiency point moves toward the direction of small flow. Based on the mixture multiphase flow model. Zhang *et al.* (2013, 2014) found a clear jet-wake structure near the volute tongue that became apparent as the volume fraction increased. Harry *et al.* (2005) obtained different wear forms of the centrifugal pump blade when the mud was conveyed. Veselin *et al.* (2010) proposed a wear prediction method based on rapid experiment and mathematical analysis; the method replaced the traditional mud pump wear test that was time consuming, consumptive, and unsuitable. The error between prediction and experiment was less than 3%. Pagalthivarthi *et al.* (2011) studied the effect of operating parameter, pump flow, rotation rate, particle diameter and shape, volute tongue curvature, and volute width on particle erosion wear through numerical computation. Dong *et al.* (2009) found that flow parameters, such as particle size and shape as well as liquid velocity, significantly influence the surface erosion pits of over-current components, and the twist degree and the maximum stress increases along with the enlargement of particles. Li *et al.* (2010) revealed the effect of internal flow characteristics on the wear characteristics of solid–liquid two-phase centrifugal pump. Moreover, more flow characteristics inside pump has been revealed deeply (Cheng *et al.*, 2022; Cheng and Zhang, 2022).

However, with the extensive application of solid–liquid pump, its shortcomings in practical application are gradually exposed, such as the severe wear and low efficiency of over-current components. Due to the complexity of two-phase flow, the theoretical research and design on this aspect remain immature and are still in the exploration stage, and the development and some principles of solid–liquid two-phase flow in the passageway have not been revealed. This research performs numerical simulation and analysis on a solid–liquid two-phase flow pump and analyzes the effect of the diameter of solid particles on the internal flow characteristics of the sewage pump. The basic characteristics of the sewage pump are preliminarily predicted, which lay a theoretical basis for the subsequent improvement.

2. PUMP MODEL AND METHOD

2.1 Pump model and mesh

The pump model is a medium-speed centrifugal pump with a specific speed n_s = 129.3. The basic performance parameters of the pump are as follows: flow Q = 50 m^3/h, head H = 20.54 m, speed n = 2900 r/min. The main geometric dimensions of the pump include the following: diameter of pump inlet D_j = 76 mm, hub diameter dh = 0 mm, diameter of impeller outlet D_2 = 137 mm, width of impeller outlet b_2 = 14 mm, angle of blade outlet β_2 = 30°, number of blade Z = 6, wrap angle φ = 104.5°, diameter of volute base D_3 = 145 mm, width of volute inlet b_3 = 30 mm.

2.2 Computation mesh

The mesh is divided in the computation domain by the commercial

* *Corresponding author. Email: zhang002@sina.com*

Global Digital Central
ISSN: 2151-8629

meshing software GAMBIT2.3.16, as shown in Fig. 1. The tetrahedral mesh is used in the impeller rotation zone and the volute still zone; he total number of the mesh in the computing domain is 1240428. The number of mesh is not adequate for the fine flow in the simulated boundary layer but sufficient for simulating the macro-flow of the pump and capturing the macroscopic characteristics of the pump. Mesh quality inspection reveals that the equiangular slope and the equal slope are not more than 0.83, the near wall Y + is approximately 30, and the mesh is of good quality.

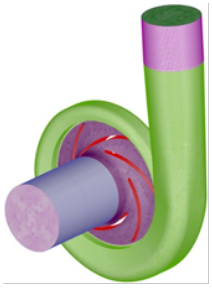

Fig. 1 Computation mesh

2.3 Governing equations

The 3D unsteady turbulence of incompressible fluid inside the centrifugal pump can be presented in the Renault mean equation.

$$\begin{cases} \dfrac{\partial \overline{u}_i}{\partial x_i} = 0 \\ \rho\dfrac{\partial \overline{u}_i}{\partial t} + \rho\overline{u}_j\dfrac{\partial \overline{u}_i}{\partial x_j} = \rho F_i - \dfrac{\partial \overline{p}}{\partial x_i} + \mu\dfrac{\partial^2 \overline{u}_i}{\partial x_j \partial x_j} - \rho\dfrac{\partial}{\partial x_j}\left(\overline{u_i' u_j'}\right) \end{cases} \tag{1}$$

where ρ is the fluid density, and $-\rho\overline{u_i' u_j'}$ represents the average Reynolds stress. u_i is the instantaneous velocity.

According to Boussinesq hypothesis,

$$-\rho\overline{u_i' u_j'} = \mu_t\left(\frac{\partial \overline{u}_i}{\partial x_j} + \frac{\partial \overline{u}_j}{\partial x_i}\right) - \frac{2}{3}\left(\rho k + \mu_t\frac{\partial \overline{u}_i}{\partial x_i}\right)\delta_{ij} \tag{2}$$

Where μ_t is the turbulence viscosity coefficient, and it is the function of the turbulence k and the turbulence dissipation coefficient ε.

The RNG k-ε two-equation model is used in the unsteady turbulence computation to make the Renault mean equation closed. The RNG k-ε turbulence model considers the rotation and swirl flow in the average flow, which can efficiently dispose the high strain rate and the flow of large streamline bending. Its form is as follows:

$$\rho\frac{\mathrm{d}k}{\mathrm{d}t} = \frac{\partial}{\partial x_j}\left(\alpha_k\mu_{\mathrm{eff}}\frac{\partial k}{\partial x_j}\right) + 2\mu_t\overline{\boldsymbol{S}}_{ij}\frac{\partial \overline{u}_i}{\partial x_j} - \rho\varepsilon \tag{3}$$

$$\rho\frac{\mathrm{d}\varepsilon}{\mathrm{d}t} = \frac{\partial}{\partial x_j}\left(\alpha_\varepsilon\mu_{\mathrm{eff}}\frac{\partial \varepsilon}{\partial x_j}\right) + 2C_{1\varepsilon}\frac{\varepsilon}{k}\nu_t\overline{\boldsymbol{S}}_{ij}\frac{\partial \overline{u}_i}{\partial x_j} - C_{2\varepsilon}\rho\frac{\varepsilon^2}{k} - R \tag{4}$$

Where $\overline{\boldsymbol{S}}_{ij} = \frac{1}{2}\left(\frac{\partial \overline{u}_i}{\partial x_j} + \frac{\partial \overline{u}_j}{\partial x_i}\right)$; $\mu_{\mathrm{eff}} = \mu + \mu_t$; $\mu_t = C_\mu\frac{k^2}{\varepsilon}$; $\overline{\boldsymbol{S}}_{ij}$ is the strain rate tensor; R is the additional source term in the ε equation, which represents the effect of average strain rate ε and has the following expression:

$$R = \frac{C_\mu\eta^3(1-\eta/\eta_0)}{1+\beta\eta^3}\frac{\varepsilon^2}{k}, \eta = Sk/\varepsilon \tag{5}$$

The model parameters in the above equation are $C_\mu = 0.0845$, $C_{1\varepsilon} = 1.42$, $C_{2\varepsilon} = 1.68$, $\alpha_k = 1.0$, $\alpha_\varepsilon = 0.769$, $\beta = 0.012$, and $\eta_0 = 4.38$.

2.4 Mixture model

In this study, 3D turbulent flow computation of incompressible viscous fluid is conducted through business code-FLUENT software based on finite volume method (Malek *et al.*, 2019; Malek *et al.*, 2019). The algebraic slip mixture model (ASMM) based on Euler–Euler method is used to calculate the solid–liquid two-phase flow in the numerical computation of multiphase flow model (Sanyal *et al.*, 1999). The particle equivalent is taken as quasi-fluid.

The general form of the ASMM is as follows, i.e., continuity equation,

$$\frac{\partial}{\partial t}(\rho_m) + \frac{\partial}{\partial x_i}(\rho_m\boldsymbol{u}_{m,i}) = 0 \tag{6}$$

where ρ_m is the density of the mixture, and u_m is the mass average velocity.

The momentum equation is

$$\begin{aligned} \frac{\partial}{\partial t}(\rho_m u_{m,j})\frac{\partial}{\partial x_i}(\rho_m u_{m,i}u_{m,j}) = -\frac{\partial p}{\partial x_j} + \frac{\partial}{\partial x_i}\times\mu_m\left(\frac{\partial u_{m,i}}{\partial x_j} + \frac{\partial u_{m,j}}{\partial x_i}\right) \\ + \rho_m g_j + \boldsymbol{F}_j + \frac{\partial}{\partial x_i}\left(\sum_{k=1}^{n}\varphi_k\rho_k u_{D,k,i}u_{D,k,j}\right) \end{aligned} \tag{7}$$

where p is the pressure, μ_m is the effective viscosity of the mixture, g is the gravitational acceleration, F is the volume force, φ is the volume fraction, and $u_{D,k}$ is the drift velocity.

The volume fraction equation is

$$\frac{\partial}{\partial t}(\varphi_s\rho_s) + \frac{\partial}{\partial x_i}(\varphi_s\rho_s u_{m,i}) = -\frac{\partial}{\partial x_i}(\varphi_s\rho_s u_{D,s,i}) \tag{8}$$

$$\rho_m = \sum_{k=1}^{n}\varphi_k\rho_k \quad \mu_m = \sum_{k=1}^{n}\varphi_k\mu_k \quad \boldsymbol{u}_m = \left(\sum_{k=1}^{n}\varphi_k\rho_k\boldsymbol{u}_k\right)/\rho_m \tag{9}$$

The drift speed of k-phase is

$$\boldsymbol{u}_{D,k} = \boldsymbol{u}_k - \boldsymbol{u}_m = \boldsymbol{v}_{k,c} - \frac{1}{\rho_m}\sum_{i=1}^{n-1}\varphi_i\rho_i\boldsymbol{v}_{i,c}u \tag{10}$$

The slip rate of k-phase is

$$\boldsymbol{v}_{k,c} = \frac{(\rho_m-\rho_k)d_k^2}{18\mu_c\mu}\left[\left(\boldsymbol{g} - \frac{D\boldsymbol{u}_m}{Dt}\right)\right] \tag{11}$$

$$\mu = \begin{cases} 1+0.05Re^{0.687} & Re < 1\ 000 \\ 0.018Re & Re \geq 1\ 000 \end{cases} \tag{12}$$

where μ is the friction factor, d is the particle diameter, μ_c is the continuous-phase viscosity, and Re is the local Reynolds number. In this study, the calculated medium is a solid–liquid two-phase flow, where $n = 2$. If a steady flow computation is to be conducted, the phase of the local change rate will no longer exist in the above equation.

2.5 Solution settings

The dynamic and static coupling in the numerical computation is realized by the "frozen rotor method." The velocity inlet and free discharge are used as boundary conditions for the inlet and outlet,

respectively. The axial velocity of the pump inlet is calculated directly according to the given flow conditions and the diameter of the pump inlet. The turbulent kinetic energy and turbulent dissipation rate are then calculated according to the axial velocity and the diameter of the pump inlet. The non-slip boundary conditions are applied at all solid walls considering the cause of viscosity. The problem of the high-Reynolds-number turbulence model is treated by the standard wall function in the near-wall low-Reynolds-number region.

With the design discharge (Q = 50 m^3/h). The solid concentration is 10%, the density is 2500 kg/m^3, the diameters of particles are 0.01, 0.05, 0.10, 0.15, and 0.20 mm, and the solid–liquid two-phase flow field is numerically calculated.

3. RESULTS ANALYSIS

3.1 Turbulence flow characteristics of pressure surface

Fig. 2 shows the distribution of individual physical quantity on the pressure surface. For the turbulent kinetic energy, Fig.2(a) shows that as the particle diameter enlarges, the turbulent kinetic energy tends to decrease gradually, which indicates that the pulsation is less and that large particles have a good effect on controlling turbulence pulsation. For any of the five particle diameters, the turbulent kinetic energy is always the largest at the front edge of the blade pressure surface, rapidly declines, then rises continuously, and drops again near the outlet.

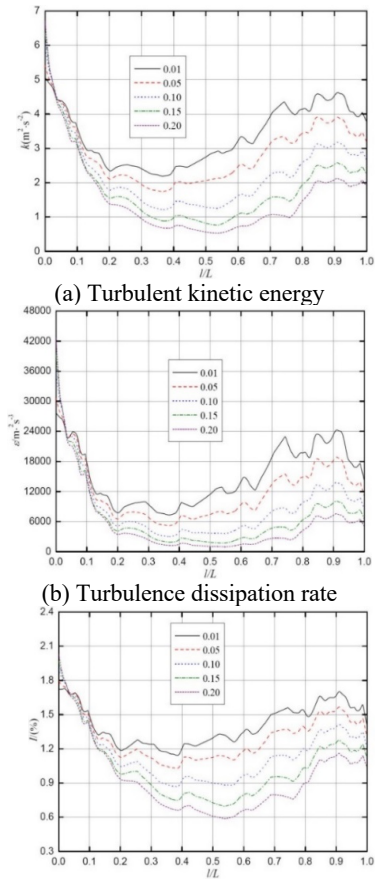

(a) Turbulent kinetic energy

(b) Turbulence dissipation rate

(c) Turbulence intensity

Fig. 2 Effect of particle diameter on turbulence flow characteristics of blade pressure surface

The computation results show that the turbulent kinetic energies corresponding to the five particle diameters are 5.06, 5.41, 5.99, 6.37, and 6.71 m2·s−2 at a relative length of 0, i.e., the front edge of the blade pressure surface. Meanwhile, the turbulent kinetic energies corresponding to the five particle diameters are 3.77, 3.18, 2.66, 2.23, and 1.90 m2·s−2 at a relative length of 1, i.e., the outlet of the blade pressure surface. In the middle of the blade pressure surface, the turbulent kinetic energies corresponding to the five particle diameters are 2.75, 2.06, 1.28m, 0.81, and 0.56 m2·s−2. Fig.2(b) and Fig.2(c) show that the variation characteristics of turbulence dissipation rate and turbulence intensity are generally similar to those of turbulent kinetic energy, that is, the turbulence dissipation rate and turbulence intensity are always the largest at the front edge of the blade pressure surface, rapidly declines, then rises continuously, and drops again near the outlet. In general, the variation characteristics of turbulent kinetic energy, turbulence dissipation rate, and turbulence intensity reflect the characteristics of turbulent flow.

3.2 Turbulence flow characteristics of suction surface

Fig. 3 shows the distribution of physical quantities on the suction surface. Given that the turbulent kinetic energy, turbulent dissipation rate, and turbulent intensity variation on the blade pressure surface are similar, the turbulent kinetic energy (Fig.3(a)), turbulence dissipation rate (Fig.3(b)), and turbulence intensity variation (Fig.3(c)) on the blade suction surface are also similar. With the enlargement of the particle diameter, the three physical quantities show a gradual increasing trend.

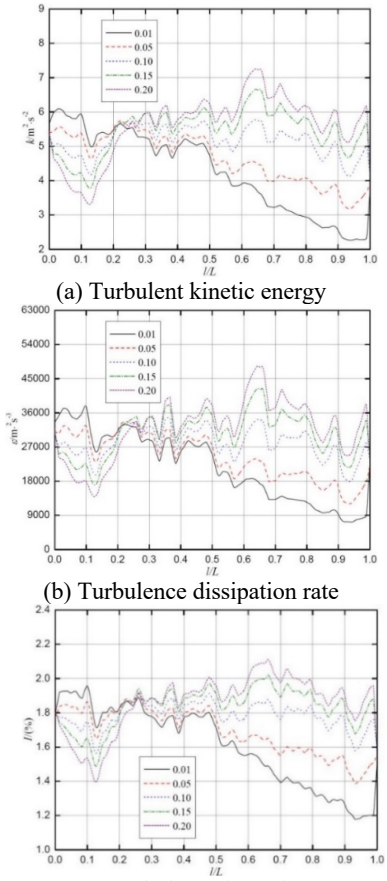

(a) Turbulent kinetic energy

(b) Turbulence dissipation rate

(c) Turbulence intensity

Fig. 3 Effect of particle diameter on turbulence flow characteristics of blade suction surface

3.3 Particle concentration distribution on a blade surface

Fig.4 shows the change in the particle concentration distribution on a blade surface with different particle diameters. In the case of five particle diameters, the concentration of solid particles on the blade suction surface is evidently higher than that on the blade pressure surface. The wear on the blade suction surface is more severe than that on the blade pressure surface, considering that the solid-phase concentration reflects the wear degree of the wall surface to a certain extent. Nonetheless, the computation result also reflects some differences. When the relative length is less than 0.12, that is, at the

blade inlet, the solid-phase concentration on the blade pressure surface is higher than that on the blade suction surface, which indicates that the wear on the blade pressure surface is more severe. The solid-phase concentration on the blade pressure surface changes slightly as the blade radius enlarges.

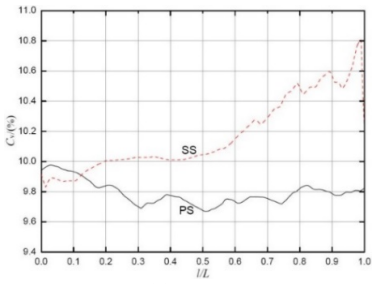

(a) 0.01mm

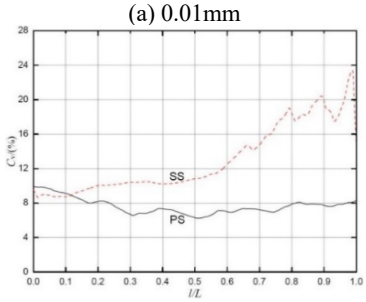

(b) 0.05mm

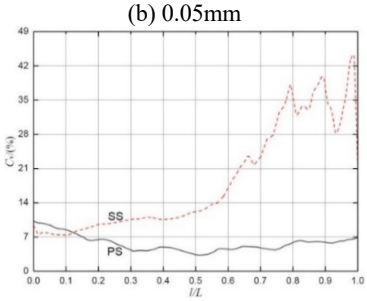

(c) 0.10mm

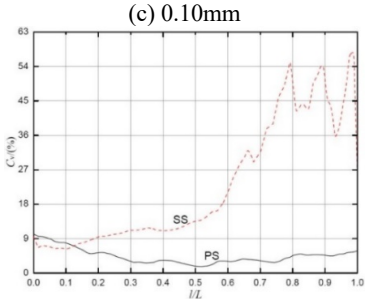

(d) 0.15mm

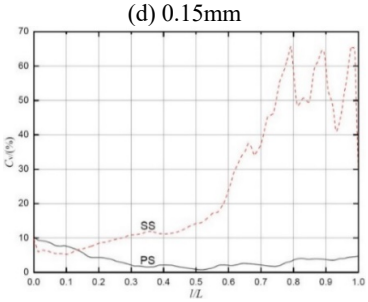

(c) 0.20mm

Fig. 4 Particle concentration distribution on a blade surface with different particle diameters

3.4 Particle concentration on the blade pressure surface

Fig. 5 depicts the change in the particle concentration distribution on the pressure surface of blades with different particle diameters. When the particle diameter is 0.01 mm, the solid concentration distribution on the entire pressure surface is more uniform; when the particle diameter is 0.05 mm, the solid-phase concentration on the pressure surface near the front and rear covers is low, whereas that in the middle is high. When the particle diameter is 0.10 mm, the low-concentration area near the front and rear covers on the pressure surface expands continuously; when the particle diameters are 0.15 mm and 0.20 mm, the low-concentration area occupies most of the area of the blade pressure surface; a high concentration of solid particles is observed at the blade inlet.

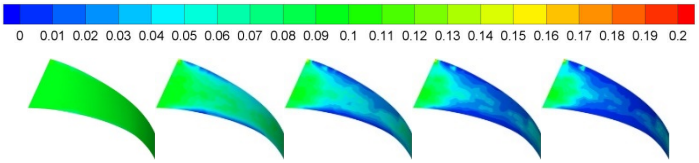

(a) 0.01mm (b) 0.05mm (c) 0.10mm (d) 0.15mm (e) 0.20mm

Fig. 5 Particle concentration distribution on pressure surface of blades with different particle diameters

3.5 Particle concentration on the blade suction surface

Fig.6 shows the change in the particle concentration distribution on the suction surface of blades with different particle diameters. When the particle diameter is 0.01 mm, the distribution of solid-phase concentration on the entire suction surface is relatively uniform, and that at the blade inlet is high. When the particle diameter is 0.05 mm, the distribution gradually enlarges from the blade outlet. When the particle diameters are 0.10, 0.15, and 0.20 mm, the solid-phase concentration near the front cover on the suction surface is high, and that at the outlet is also high, indicating that the wear is more severe.

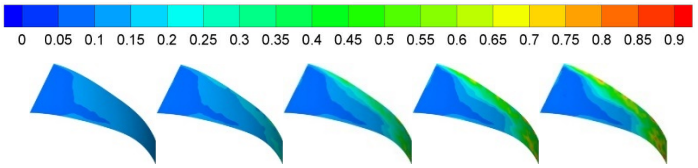

(a) 0.01mm (b) 0.05mm (c) 0.10mm (d) 0.15mm (e) 0.20mm

Fig. 6 Particle concentration distribution on suction surface of blades with different particle diameters

3.6 Particle concentration on the volute surface

Fig.7 indicates the change in the particle concentration distribution on the volute surface of blades with different particle diameters.

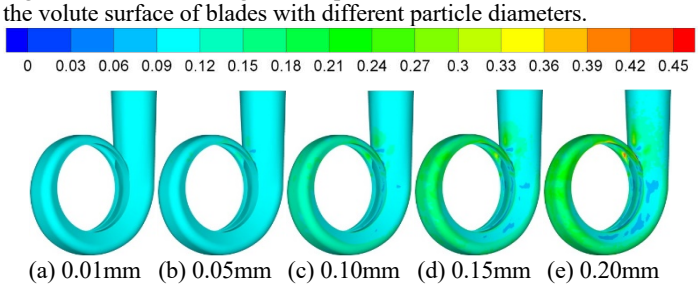

(a) 0.01mm (b) 0.05mm (c) 0.10mm (d) 0.15mm (e) 0.20mm

Fig. 7 Particle concentration distribution on volute surface of blades with different particle diameters

When the particle diameters are 0.01 mm and 0.05 mm, the difference in the distribution of solid-phase concentration on the volute surface is not evident, mainly because the particles are so small that the subsequent performance of particles following the water flow is good. When the particle diameter is 0.10 mm, the solid-phase concentration on the volute surface is high, and the wear is more severe. When the particle diameters are 0.15 mm and 0.20 mm, the solid-phase concentration on the volute surface is significantly higher, especially when the over-current cross section enlarges constantly.

3.7 Total pressure and flow line

Fig.8 shows the distribution of total pressure and flow line of blades with different particle diameters. In the case of different particle diameters, the difference in flow line in each flow passage is not evident, mainly because the operating conditions of computation can be taken as the operating conditions of design and the internal flow is generally good.

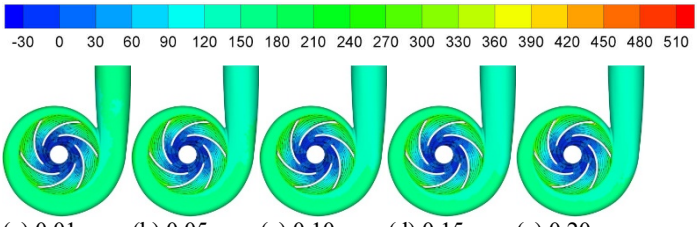

(a) 0.01mm (b) 0.05mm (c) 0.10mm (d) 0.15mm (e) 0.20mm

Fig. 8 Distribution of total pressure and flow line in the case of different particle diameters

4. CONCLUSIONS

When the particle diameters are 0.01 mm and 0.05 mm, the difference in the distribution of solid-phase concentration on the volute surface is not evident. When the particle diameter is 0.01 mm, the solid-phase concentration on the blade suction surfaces changes slightly. When the particle diameter is 0.10 mm, the solid-phase concentration on the volute surface is high, and the wear is more severe. The change in particle diameter has an insignificant effect on the change in total pressure at the first half of the blade suction surface.

ACKNOWLEDGEMENTS

The research was financially supported by Science and Technology Project of Quzhou (Grant No.2022K98).

REFERENCES

Cheng, L., and Zhang, Y.L., 2022, “Self-coupling numerical calculation of centrifugal pump startup process,” *Frontiers in Heat and Mass Transfer*, 18, 26.1-6.
http://dx.doi.org/10.5098/hmt.18.26

Cheng, L., Zhang, Y.L., and Li, J.F., 2022, “Diagnosis of Centrifugal Pump Speed Fluctuation by Using Vortex Dynamics,” *Frontiers in Heat and Mass Transfer*, 19, 32.1-7.
http://dx.doi.org/10.5098/hmt.19.32

Dong, X., Zhang, H.L., Wang, X.Y., 2009, Finite element analysis of wear for centrifugal slurry pump. *The 6th International Conference on Mining Science & Technology*, (1): 1532-1538.
https://doi.org/10.1016/j.proeps.2009.09.236

Engin, T., Gur, M., 2001, Performance characteristics of centrifugal pump impeller with running tip clearance pumping solid-liquid mixtures. *Journal of Fluids Engineering*, 123(3): 532-538.
https://doi.org/10.1115/1.1379034

Gandhi, B.K., Singh, S.N., Seshadn, V., 2002, Effect of speed on the performance characteristics of a centrifugal slurry pump. *Journal of Hydraulic Engineering*, 128(2): 225-233.
https://doi.org/10.1061/(ASCE)0733-9429(2002)128:2(225)

Harry, H.T., Graeme, R.A., 2005, Experimental study on erosive wear of some metallic materials using Coriolis wear testing approach. *Wear*, (258): 458-469.
https://doi.org/10.1016/j.wear.2004.09.002

Li, Y., Zhu, Z.C., He, W.Q., et al., 2012, Numerical simulation and experimental research on the influence of solid phase characteristics on centrifugal pump performance. *Chinese Journal of Mechanical Engineering*, 25(6): 1184-1189.
https://doi.org/10.3901/CJME.2012.06.1184

Li, Y., Zhu, Z.C., He, Z.H., et a1., 2010, Abrasion characteristic analyses of solid-liquid two-phase centrifugal pump. *Journal of Thermal Science*, 20(3): 283-287.
https://doi.org/10.1007/s11630-011-0471-8

Malek, M., Izem, N., Seaid, M., et al., 2019, A partition of unity finite element method for nonlinear transient diffusion problems in heterogeneous materials. *Computational and Applied Mathematics*, 38(2), 31.
https://doi.org/10.1007/s40314-019-0782-z

Malek, M., Izem, N., Mohamed, M.S., et al., 2019, "A partition of unity finite element method for three-dimensional transient diffusion problems with sharp gradients. *Journal of Computational Physics*, 396: 702-717.
https://doi.org/10.1016/j.jcp.2019.06.062

Pagalthivarthi, K.V., Gupta, P.K., Tyagi, V., et al., 2011, CFD prediction of erosion wear in centrifugal slurry pumps for dilute slurry flows. *Journal of Computational Multiphase Flows*, 3(4): 225-245.
https://doi.org/10.1260/1757-482X.3.4.225

Sanyal, J., Vasquez, S., Roy, S., et al., 1999, Numerical simulation of gas-liquid dynamics in cylindrical bubble column reactors. *Chemical Engineering Science*, 54(21)：5071-5083.
https://doi.org/10.1016/S0009-2509(99)00235-3

Veselin, B., 2010, Erosive wear model of slurry pump impeller. *Journal of Tribology*, 132(2): 021602.1～5.
https://doi.org/10.1115/1.4001167

Yuan, S.Q., Zhang, P.F., Zhang, J.F., 2004, Numerical simulation of 3-D dense solid- liquid two- phase turbulent flow in a non-clogging mud pump. *Chinese Journal of Mechanical Engineering*, 17(4):623-627.

Zhang, Y.L., Li, Y., Cui B.L., et al., 2013, Numerical simulation and analysis of solid-liquid two-phase flow in centrifugal pump. *Chinese Journal of Mechanical Engineering*, 26(1): 53-60.
https://doi.org/10.3901/CJME.2013.01.053L.

Zhang, Y.L., Li, Y., Zhu, Z.C., et al., 2014, Computational analysis of centrifugal pump delivering solid-liquid two-phase flow during startup period. *Chinese Journal of Mechanical Engineering*, 27(1): 178-185.
https://doi.org/10.3901/CJME.2014.01.178